Bi-cubic scaffold surfaces

Kęstutis Karčiauskas[a], Jörg Peters[b,*]

Department CISE, University of Florida

[a] *Vilnius University, Lithuania*
[b] *University of Florida, USA*

Abstract

Scaffold-like surfaces, ranging from large-scale trusses to engineered micro-structures, are often sketched via repeating patterns of nodes and edges. Offsetting these graphs turns them into meshes for which a smoothly-rounded scaffold surface 'skin' needs to be locally generated on the fly for production or analysis. We focus on minimal single-valence (MSV) quad meshes whose irregular vertices all have the same valence n and closest pairs are separated by exactly one regular, 4-valent vertex. Though at a first glance rather special, MSV meshes can model various micro-structures or trusses that occur in CAD or biology. Remarkably, bi-cubic patches provide a smooth skin of high quality, in many practical configurations with just one patch per quad.

Keywords: scaffold surface, minimal single-valence mesh, smooth surface, graph micro structure, truss rounding

---

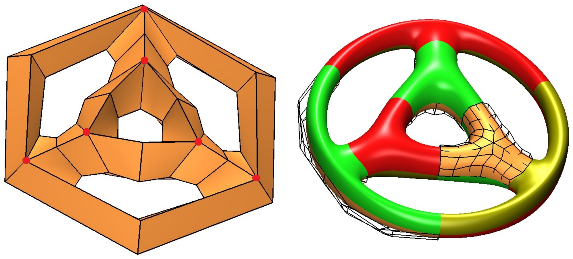

(a) MSV net

(b) layout of n-sided caps

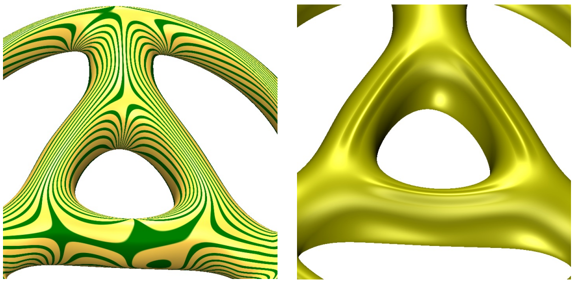

(c) highlight lines

(d) added semi-crease

Figure 1: Bi-3 scaffold surface from an MSV net with irregular node valence $n = 6$. (a) Irregular nodes marked ●. (b) Layout of differently-colored caps of the scaffold surface, some with superimposed Bézier nets. (c) highlight line distribution [1] (d) Semi-crease added by localized refinement.

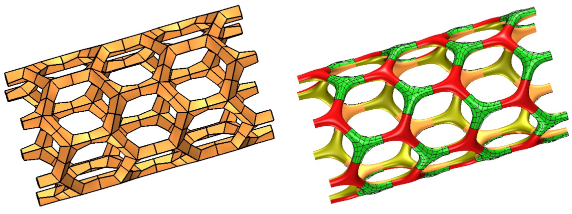

(a) MSV net

(b) layout

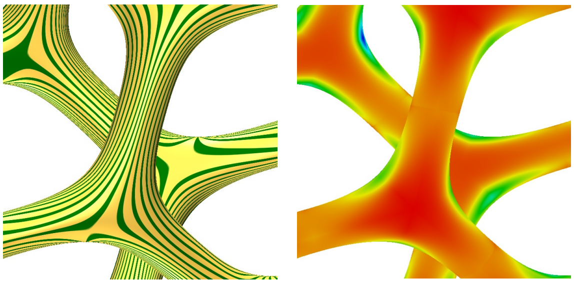

(c) highlight lines

(d) Gauss curvature

Figure 2: Bi-3 tube-scaffold surface from a valence $n = 6$ MSV net.

1. Introduction

Repeated patterns, in biology or in CAD design, often inherit their structure from an underlying graph. Examples are DNA strands, nanotubes, octet-truss, 3D Kagome lattices etc. Offsetting the edges and nodes of such graphs yields quad-faceted beams with a special connectivity pattern: irregular nodes of a single, fixed valence n are tightly packed together, separated only by one regular, 4-valent vertex. Fig. 1 a and Fig. 2 a illustrate the variety of structures already for one fixed valence $n = 6$. Other shapes, not necessarily from graphs, and with valences ranging from $n = 3$ to $n = 10$, are discussed in the body of this paper. In [2], Karciauskas and Peters named this class of meshes, characterized by vertices of a single irregular valence n separated by one regular 4-valent vertex, *minimal single-valence* (MSV) meshes. They introduced a corresponding class of scaffold surfaces and, in the case $n = 3$, sphere-like surfaces. Remarkably, these surfaces are even curvature continuous (G^2). But, while the existence of G^2 surfaces consisting of bi-quartic (degree bi-4) polynomial pieces is mathematically impressive, and a smooth join of curved structures improves their integrity under forces, curvature continuity is often not needed for scaffold surfaces. For large MSV scaffolds and where G^1 smoothness suffices, a reduction of degree, number of pieces ([2] uses macro-patches) and

---

[*] Corresponding author

Email addresses: `kestutis.karciauskas@mif.vu.lt` (Kęstutis Karčiauskas), `jorg.peters@gmail.com` (Jörg Peters)

Preprint submitted to Elsevier *July 1, 2022*

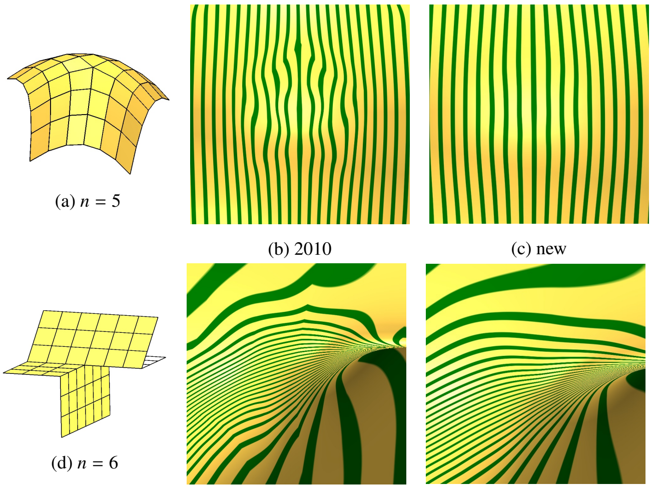
(a) $n = 5$

(b) 2010

(c) new

(d) $n = 6$

(e) 2010

(f) new

Figure 3: Progress in bi-3 surface quality (2010=[4]).

complexity of construction is most welcome. In contrast to the bi-4 macro-patch G^2 of [2] our bi-3 G^1 surfaces can be presented compactly by explicit formulas (rather than as the solution of a system of equations), and yet, for typical MSV meshes, the resulting surface quality is very similar to its curvature continuous cousin, see Fig. 2 c,d. We say remarkable because, for regular tensor-product splines, uniform highlight line and curvature distribution are typically equated to high differentiability: C^2 continuity seems to be a prerequisite for good shape of bi-cubics. Conversely, for bi-3 patches arranged in an irregular, non-tensor-product layout, non-separability and interlinking of the derivative constraints along polynomial boundaries has been shown to overly constrain the surfaces, see e.g. [3]. For our new scaffold surfaces, neither issue is of concern.

The noteworthy contributions therefore are

- a bi-cubic (minimal degree) scaffold surface with either 2×2 pieces for strongly twisted MSV nets or
- one (minimal number) bi-cubic piece per quad of the MSV net,
- both defined by an explicit set of (minimal) formulas that do not require assembling and solving a system of equations at run time.

1.1. Related work

Generating quad meshes from graphs is itself an interesting problem, see e.g. [5, 6, 7, 8]. For MSV nets, the challenge is much reduced: due to the repeating pattern and known incidence count, basic units can be glued together.

For an overview of surface constructions, see the recent survey [9] that classifies constructions for general modeling into transfinite interpolation using rational multi-sided surfaces [10, 11, 12, 13, 14], subdivision surfaces, e.g. [15], constructions with vertex singularity, e.g. [16], and geometrically continuous splines (G-splines) that assemble a finite number of polynomial piece to join smoothly after a change of variables, see e.g.[17, 18, 19, 20, 21]. [22] proved that G-splines are directly suitable for isogeometric analysis [23] also for unstructured layout [3, 24, 25]. Fig. 3 illustrates the improvement of smooth bi-3 free-form G-spline constructions from a decade ago: compare Fig. 3 b vs c and e vs f. For general input, like Fig. 3 a,d, the new scaffold-specific construction yields good highlight line distributions but formally C^0 surfaces with minimal normal deviation akin to [26]. By contrast to [26], our scaffold surfaces have explicit formulas, hence are simpler to implement, and are G^1 for MSV input, i.e. do not have the limitations pointed out in [27].

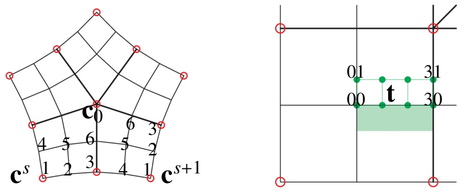

(a) CC-net

(b) Hermite **t** of degree 3

Figure 4: For MSV, the nodes marked ○ must have the same valence n as the central irregular node $\mathbf{c}_0$. (a) The CC-net of valence $n = 5$ consists of $\mathbf{c}_0$ and $6n$ nodes $\mathbf{c}_i^s$, $i = 1, \ldots, 6$, $s = 0, \ldots, n-1$. (b) First-order tensor-border $\mathbf{t}$ of degree 3 with BB-coefficients $\mathbf{t}_{ij}$, along one boundary segment, not touching an n-valent node.

Overview Section 2 develops an auxiliary bi-4 surface that simplifies the remaining work. Section 3 defines both the 2 × 2 patch per sector and the single patch bi-3 constructions. Section 4 compares options and points out subtle differences between 2×2 and single patch scaffold surfaces.

2. An (auxiliary) *n*-sided surface cap of degree bi-4

An auxiliary bi-quartic (bi-4) cap determines the shape and other key properties of the final bi-cubic (bi-3) scaffold surfaces. The input to the construction of the bi-4 cap is a network of quadrilateral (quad) faces, called *CC-net*, see Fig. 4 a, serves as input for corresponding surface pieces, called *caps*, whose union, one per n-valent point, is the scaffold surface. The central n-valent node $\mathbf{c}_0$ of the CC-net is surrounded by regular nodes and, for now, we do not restrict the valence of the second layer of nodes. (For MSV meshes every second node of the second layer, marked by ○, must be of the same valence n). We construct the auxiliary cap from n tensor-product patches of bi-degree $d = 4$ (bi-4) in Bernstein-Bézier form (BB-form, [28, 29]). That is, for Bernstein polynomials $B_k^d(t) := \binom{d}{k}(1-t)^{d-k}t^k$ of degree $d = 4$:

$$\mathbf{p}(u,v) := \sum_{i=0}^{d}\sum_{j=0}^{d} \mathbf{p}_{ij} B_i^d(u) B_j^d(v), \qquad 0 \le u, v \le 1.$$

Connecting the *BB-coefficients* $\mathbf{p}_{ij} \in \mathbb{R}^3$ to $\mathbf{p}_{i+1,j}$ and $\mathbf{p}_{i,j+1}$ wherever well-defined yields the *BB-net*. This is illustrated in Fig. 5 b for two pieces of the cap; the superscript $s \in \{0, \ldots, n-1\}$ counts the n sectors of a cap modulo n.

To smoothly join the sectors of the cap, we relate the BB-coefficients of neighboring sectors $\grave{\mathbf{p}} := \mathbf{p}^s$ and $\acute{\mathbf{p}} := \mathbf{p}^{s+1}$, $s = 0, \ldots, n-1$ by setting the coefficients $\grave{\mathbf{p}}_{ij} := \mathbf{p}^s_{4-j,4-i}$ and $\acute{\mathbf{p}}_{ij} := \mathbf{p}^{s+1}_{4-i,4-j}$, $i = 0, \ldots, 4$, $j = 0, 1$; see Fig. 5 a. The polynomial pieces join G^1 along the common sector-separating curve $\grave{\mathbf{p}}(u,0) = \acute{\mathbf{p}}(u,0)$ with BB-coefficients $\grave{\mathbf{p}}_{i0} = \acute{\mathbf{p}}_{i0}$ if, after reparameterization $\grave{\mathbf{p}}(u,v) := \acute{\mathbf{p}} \circ \rho(u,v)$, $(u,v) \in [0..1]^2$, see e.g. [30],

$$\partial_v \grave{\mathbf{p}} = a(u)\partial_v \acute{\mathbf{p}} + b(u)\partial_u \grave{\mathbf{p}} \qquad \mathsf{c} := \cos\frac{2\pi}{n}, \qquad (1)$$

$$\rho(u,v) := (u + b(u)v, a(u)v), \qquad a(u) := -1, b(u) := 2\mathsf{c}(1-u).$$

Due to $a(u) := -1$, the sectors are treated symmetrically. We enforce (1) by setting

$$\acute{\mathbf{p}}_{01} := -\grave{\mathbf{p}}_{01} + 2\mathsf{c}\grave{\mathbf{p}}_{10} + 2(1-\mathsf{c})\grave{\mathbf{p}}_{00}; \tag{2}$$

$$\grave{\mathbf{p}}_{20} := \frac{(3\mathsf{c}-4)\grave{\mathbf{p}}_{10} + 2(\grave{\mathbf{p}}_{11} + \acute{\mathbf{p}}_{11})}{3\mathsf{c}}; \tag{3}$$

$$\acute{\mathbf{p}}_{21} := -\grave{\mathbf{p}}_{21} + (2-\mathsf{c})\grave{\mathbf{p}}_{20} + \mathsf{c}\grave{\mathbf{p}}_{30}; \tag{4}$$

$$\grave{\mathbf{p}}_{30} := \frac{2(\grave{\mathbf{p}}_{31} + \acute{\mathbf{p}}_{31}) - \mathsf{c}\grave{\mathbf{p}}_{40}}{4-\mathsf{c}}; \tag{5}$$

$$\grave{\mathbf{p}}_{40} := \frac{\grave{\mathbf{p}}_{41} + \acute{\mathbf{p}}_{41}}{2}. \tag{6}$$

To smoothly join the cap to the surrounding surface, we interpret the CC-net as bi-3 B-spline coefficients and convert the B-splines to BB-form for the BB-coefficients marked as ● in Fig. 4 b. This representation of first-order Hermite data of degree 3 in BB-form is called a *tensor-border* $\mathbf{t}$. While $\mathbf{t}$ is consistent with (6), we have to reparameterize to enforce (5). Anticipating the need for C^1 joining of adjacent scaffold caps, we choose

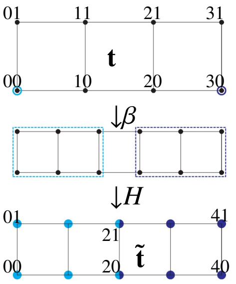

Figure 6: Transformation $H^\beta := H \circ \beta$ of input tensor-border $\mathbf{t}$ of degree 3 to tensor-border $\tilde{\mathbf{t}}$ of degree 4.

$$\beta(u,v) := (u, a(u)v),$$

$$a(u) := B_0^2(u) + B_1^2(u) + \frac{2}{2-\mathsf{c}} B_2^2(u).$$

Then $\mathbf{t} \circ \beta$ is consistent with (5). Since the first order expansion $f(u,0) + \partial_v f|_{v=0} v$ of $f := \mathbf{t} \circ \beta$ is of degree 5 rather than the desired degree 4, we subsample as follows, see Fig. 6 . At the endpoints (● and ●), the Hermite data $\begin{pmatrix} f & \partial_u f & \partial_u^2 f \\ \partial_v f & \partial_u \partial_v f & \partial_u^2 \partial_v f \end{pmatrix}$ are expressed in BB-form of bi-degree 4. The overlapping BB-coefficients are averaged to obtain the coefficients with indices 20 and 21. The BB-coefficients $\tilde{\mathbf{t}}_{i0}$, $i = 0, \dots, 4$ and $\tilde{\mathbf{t}}_{01}$, $\tilde{\mathbf{t}}_{11}$ of the resulting bi-4 tensor-border denoted $\tilde{\mathbf{t}}$ stem directly from $\mathbf{t}$ in degree-raised form, i.e. $\tilde{\mathbf{t}}_{11} := \frac{1}{16}(\mathbf{t}_{00} + 3(\mathbf{t}_{10} + \mathbf{t}_{01}) + 9\mathbf{t}_{11})$. The remaining coefficients are

$$\tilde{\mathbf{t}}_{21} := \frac{1}{16(2-\mathsf{c})}\Big(\mathsf{c}(\mathbf{t}_{01} - \mathbf{t}_{00} + \mathbf{t}_{31} - \mathbf{t}_{30}) + (4-5\mathsf{c})\mathbf{t}_{10} + 3(4-\mathsf{c})\mathbf{t}_{11}$$
$$+ (4+\mathsf{c})\mathbf{t}_{20} + 3(4-3\mathsf{c})\mathbf{t}_{21}\Big),$$

$$\tilde{\mathbf{t}}_{31} := \frac{1}{8(2-\mathsf{c})}\Big(3(1-2\mathsf{c})\mathbf{t}_{20} + 9\mathbf{t}_{21} + (1+\mathsf{c})\mathbf{t}_{30} + 3(1-\mathsf{c})\mathbf{t}_{31}\Big),$$

$$\tilde{\mathbf{t}}_{41} := \frac{1}{2(2-\mathsf{c})}\Big((1-2\mathsf{c})\mathbf{t}_{30} + 3\mathbf{t}_{31}\Big).$$

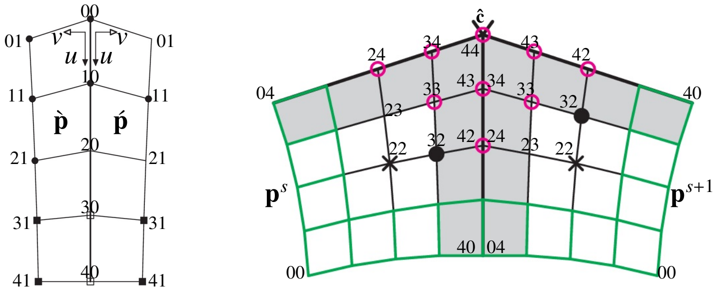

(a) local indexing

(b) global indexing

Figure 5: Indexing the BB-coefficients relevant to the G^1 constraints between adjacent bi-4 sectors.

At the central irregular point $\hat{\mathbf{c}}$, we construct a unique *quadratic expansion*, both to obtain a well-defined tangent plane at $\hat{\mathbf{c}}$ and to improve the surface quality. We define a piecewise total degree quadratic map $\mathbf{q}$ with coefficients $\mathbf{q}_k^s$, $k = 1, \dots, 6$, $s = 0, \dots, n-1$ (see see Fig. 7 a) as n pieces defined n sectors with an opening angle $\frac{2\pi}{n}$ at the origin $\mathbf{o}$ (see Fig. 7 b). The explicit formulas relating the BB-coefficients of adjacent sectors are

$$\begin{pmatrix} \mathbf{q}_1^{s+1} \\ \mathbf{q}_2^{s+1} \\ \mathbf{q}_3^{s+1} \\ \mathbf{q}_4^{s+1} \\ \mathbf{q}_5^{s+1} \\ \mathbf{q}_6^{s+1} \end{pmatrix} := \begin{pmatrix} 1 & 0 & 0 & 0 & 0 & 0 \\ 0 & 0 & 0 & 1 & 0 & 0 \\ 0 & 0 & 0 & 0 & 0 & 1 \\ 2(1-\mathsf{c}) & -1 & 0 & 2\mathsf{c} & 0 & 0 \\ 0 & 0 & 0 & 2(1-\mathsf{c}) & -1 & 2\mathsf{c} \\ 4(1-\mathsf{c})^2 & -4(1-\mathsf{c}) & 1 & 8\mathsf{c}(1-\mathsf{c}) & -4\mathsf{c} & 4\mathsf{c}^2 \end{pmatrix} \begin{pmatrix} \mathbf{q}_1^s \\ \mathbf{q}_2^s \\ \mathbf{q}_3^s \\ \mathbf{b}_4^s \\ \mathbf{q}_5^s \\ \mathbf{q}_6^s \end{pmatrix}. \tag{7}$$

Once the six BB-coefficients $\mathbf{q}_k^s$, $k = 1, \dots, 6$ of one sector s are fixed, (7) defines the BB-coefficients of the remaining sectors. The quadratic map $\mathbf{q}$ becomes the quadratic expansion of the bi-4 cap $\mathbf{p}$ at $\hat{\mathbf{c}}$ as follows. In each sector s the quadratic map $\mathbf{q}^s$ is composed with $\tau^s : [0..1]^2 \to \mathbb{R}^2$ whose BB-coefficients $\tau_{44}^s := \mathbf{o}$, τ_{43}^s and τ_{34}^s coincide with other two vertices of the domain triangle of $\mathbf{q}^s$ (light red in Fig. 7 b) and

$$\tau_{42}^s := 2\tau_{43}^s - \tau_{44}^s, \quad \tau_{24}^s := 2\tau_{24}^s - \tau_{44}^s, \tag{8}$$

$$\tau_{33}^s := \kappa(\tau_{42}^s + \tau_{24}^s) + (1-2\kappa)\tau_{44}^s, \ \kappa := \frac{4+3\mathsf{c}}{8(1+\mathsf{c})}. \tag{9}$$

Then at $\mathbf{o}$ the Hermite data $\{f, \partial_u f, \partial_v f, \partial_u^2 f\ \partial_u \partial_v f, \partial_v^2 f\}$ of the composition $f := \mathbf{q}^s \circ \tau^s$ in bi-degree 4 BB-form are, see Fig. 5 b, the magenta BB-coefficients $\mathbf{p}_{ij}^s$ of the cap sector $\mathbf{p}^s$: i.e. we have explicitly

$$\begin{pmatrix} \mathbf{p}_{44}^s \\ \mathbf{p}_{34}^s \\ \mathbf{p}_{24}^s \\ \mathbf{p}_{43}^s \\ \mathbf{p}_{33}^s \\ \mathbf{p}_{42}^s \end{pmatrix} := \begin{pmatrix} 1 & 0 & 0 & 0 & 0 & 0 \\ -1 & 2 & 0 & 0 & 0 & 0 \\ -\frac{1}{3} & -\frac{4}{3} & \frac{8}{3} & 0 & 0 & 0 \\ -1 & 0 & 0 & 2 & 0 & 0 \\ -\frac{1}{1+\mathsf{c}} & -\frac{\mathsf{c}}{2(1+\mathsf{c})} & 0 & -\frac{\mathsf{c}}{2(1+\mathsf{c})} & 2 & 0 \\ -\frac{1}{3} & 0 & 0 & -\frac{4}{3} & 0 & \frac{8}{3} \end{pmatrix} \begin{pmatrix} \mathbf{q}_1^s \\ \mathbf{q}_2^s \\ \mathbf{q}_3^s \\ \mathbf{q}_4^s \\ \mathbf{q}_5^s \\ \mathbf{q}_6^s \end{pmatrix}. \tag{10}$$

With reference to Fig. 5 b, the construction consists of the following steps.

(a) The green parts of the BB-nets (BB-subnets) are defined by the tensor-borders $\tilde{\mathbf{t}}$.

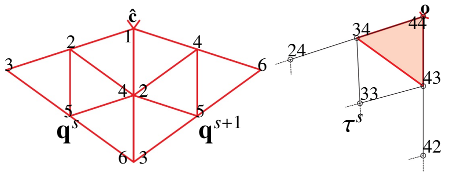

(a)

(b)

Figure 7: (a) Labeling the coefficients of quadratic map $\mathbf{q}$; (b) reparameterization τ.

(b) $\hat{\mathbf{c}}$ is chosen to be the Catmull-Clark subdivision limit point [31]

$$\hat{\mathbf{c}} := \frac{n}{n+5}\mathbf{c}_0 + \frac{1}{n(n+5)}\sum_{s=0}^{n-1}(\mathbf{c}_5^s + 4\mathbf{c}_6^s), \tag{11}$$

slightly corrected for $n = 3$ with $\gamma_5 := \frac{5}{96}$, $\gamma_6 := \frac{1}{6}$:

$$\hat{\mathbf{c}} := (1 - 3\gamma_5 - 3\gamma_6)\mathbf{c}_0 + \sum_{s=0}^{2}(\gamma_5\mathbf{c}_5^s + \gamma_6\mathbf{c}_6^s); \tag{12}$$

(c) $\mathbf{p}_{22}^s$ (marked as ×) is chosen to prevent undue oscillation. Its BB-net row and column are initialized as degree 3, degree-raised to degree 4 and averaged at $_{22}$, yielding

$$\begin{aligned}\mathbf{p}_{22}^s := \frac{1}{2}(\frac{2}{3}(\mathbf{p}_{21}^s + \mathbf{p}_{23}^s) - \frac{1}{6}(\mathbf{p}_{20}^s + \mathbf{p}_{24}^s))+ \\ \frac{1}{2}(\frac{2}{3}(\mathbf{p}_{12}^s + \mathbf{p}_{32}^s) - \frac{1}{6}(\mathbf{p}_{02}^s + \mathbf{p}_{42}^s)).\end{aligned} \tag{13}$$

(d) The remaining n unconstrained BB-coefficients $\mathbf{p}_{32}^s$ (marked as •) and the 5 coefficients of the quadratic expansion are set by minimizing the sum over the fourth derivatives, squared, of all n bi-4 patches $\mathbf{p}^s$: $\sum_{i=0}^{n-1}\mathcal{F}_4\mathbf{p}^s$ where $\mathcal{F}_k g := \int_0^1\int_0^1\sum_{i+j=k,i,j\geq 0}\frac{k!}{i!j!}(\partial_s^i\partial_t^j g(s,t))^2\, ds\, dt$.

For convenient implementation, the construction is computed for a CC-net in symbolic form, just once separately for each valence n. This expresses the BB-coefficients of each bi-4 cap patches $\mathbf{p}^s$ as a linear combination of the CC-net. It suffices to record the weights of $\mathbf{p}_{33}^0$ and $\mathbf{p}_{43}^0$. Furthermore, the number of weight digits can be reduced from the original 20 to 5 and symmetries halve the number weights to be pre-computed. This technical part is summarized in Appendix 1 and 3. The algorithm then simplifies to a sequence of assignments:

Algorithm Apply (a) and (b) above, set $\mathbf{p}_{33}^s$ and $\mathbf{p}_{43}^s$ by Appendix 1, set $\mathbf{p}_{42}^s = \grave{\mathbf{p}}_{20}$ by (3), initialize, analogous to (13), (note the superscript ~)

$$\tilde{\mathbf{p}}_{32}^s := \frac{2}{3}(\mathbf{p}_{31}^s + \mathbf{p}_{33}^s) - \frac{1}{6}(\mathbf{p}_{30}^s + \mathbf{p}_{34}^s),$$

$$\tilde{\mathbf{p}}_{23}^s := \frac{2}{3}(\mathbf{p}_{13}^s + \mathbf{p}_{33}^s) - \frac{1}{6}(\mathbf{p}_{03}^s + \mathbf{p}_{43}^s).$$

(The relation between $\mathbf{p}^s$, $\mathbf{p}^{s+1}$ and $\grave{\mathbf{p}}$, $\acute{\mathbf{p}}$ was introduced at the beginning of this section.) The smoothness between the sectors follows from (c) and the adjustment

$$\grave{\mathbf{a}}_{21} := \tilde{\mathbf{p}}_{32}^s,\ \acute{\mathbf{a}}_{21} := \tilde{\mathbf{p}}_{23}^{s+1}, \quad \breve{\mathbf{p}}_2 := (2-\mathsf{c})\grave{\mathbf{p}}_{20} + \mathsf{c}\grave{\mathbf{p}}_{30}.$$

$$\mathbf{p}_{32}^s = \grave{\mathbf{p}}_{21} := \frac{1}{2}(\grave{\mathbf{a}}_{21} - \acute{\mathbf{a}}_{21}) + \frac{1}{2}\breve{\mathbf{p}}_2,$$

$$\mathbf{p}_{23}^{s+1} = \acute{\mathbf{p}}_{21} := -\frac{1}{2}(\grave{\mathbf{a}}_{21} - \acute{\mathbf{a}}_{21}) + \frac{1}{2}\breve{\mathbf{p}}_2. \tag{14}$$

Remark. The adjustment (14) is a specific application of the following general principle. For G^1 constraints (1) with $a(u) := -1$ and $b(u)$ a linear function,

$$\acute{\mathbf{p}}_{i1} := -\grave{\mathbf{p}}_{i1} + \breve{\mathbf{p}}_i, \tag{15}$$

where $\breve{\mathbf{p}}_i$ is a linear combination of BB-coefficients of the curve shared by adjacent sectors. Then $\acute{\mathbf{p}}_{i1}$ and $\grave{\mathbf{p}}_{i1}$ satisfy (15) and, in least squares sense, minimally deviate from $\grave{\mathbf{a}}_{i1}$ and $\acute{\mathbf{a}}_{i1}$ respectively if (see Fig. 8)

$$\grave{\mathbf{p}}_{i1} := \frac{1}{2}(\grave{\mathbf{a}}_{i1} - \acute{\mathbf{a}}_{i1}) + \frac{1}{2}\breve{\mathbf{p}}_i,\ \acute{\mathbf{p}}_{i1} := -\frac{1}{2}(\grave{\mathbf{a}}_{i1} - \acute{\mathbf{a}}_{i1}) + \frac{1}{2}\breve{\mathbf{p}}_i. \tag{16}$$

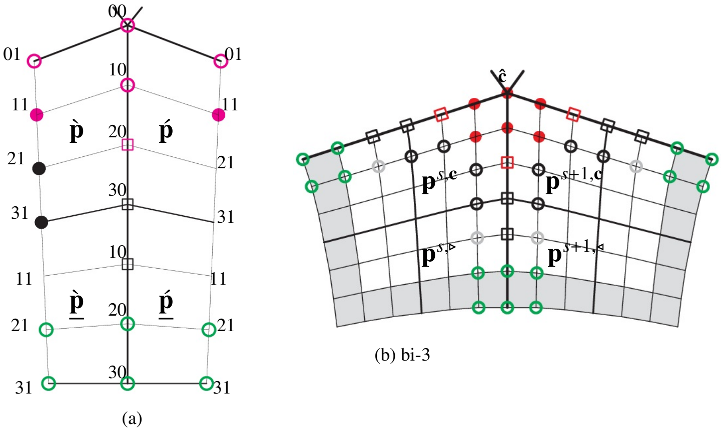

Figure 9: Indices of BB-coefficients in G^1 constraints between 2 × 2 bi-3 sectors. (b) bi-3 BB-net of two sectors. Analogous to joining bi-4 sectors, the BB-coefficients are alternatively labeled $\grave{\mathbf{p}}_{ij} := \mathbf{p}^{s,\mathbf{c}}_{3-j,3-i}$, $\acute{\mathbf{p}}_{ij} := \mathbf{p}^{s+1,\mathbf{c}}_{3-i,3-j}$, $\underline{\grave{\mathbf{p}}}_{ij} := \mathbf{p}^{s,\triangleright}_{3-j,3-i}$, $\underline{\acute{\mathbf{p}}}_{ij} := \mathbf{p}^{s+1,\triangleleft}_{3-i,3-j}$, $i = 0,\ldots,3$, $j = 0, 1$.

3. Bi-3 caps

All the hard work for constructing the bi-3 caps was already done when constructing the auxiliary bi-4 cap. Analogous to Section 2, the BB-coefficients $\mathbf{p}$ for the bi-3 cap and $\grave{\mathbf{p}}$, $\acute{\mathbf{p}}$ for the G^1 join across sectors are shown in Fig. 9 for 2 × 2 sectors and in Fig. 11 a,b for a single sector.

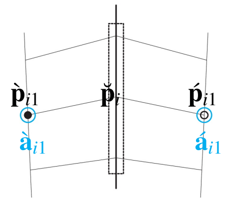

Figure 8: The BB-coefficients $\grave{\mathbf{p}}_{i1}$ and $\acute{\mathbf{p}}_{i1}$ satisfy the G^1 constraints between sectors while minimizing the distance to $\acute{\mathbf{a}}$.

3.1. 2 × 2 bi-3 patches per sector

Fig. 9 a illustrates the relations for G^1 continuity between sectors. For the top, meeting at $\hat{\mathbf{c}}$, the reparameterization is $\rho(u,v) := (u, (2\mathsf{c}(1-u)+\mathsf{c}u)v)$. For the bottom it is $\underline{\rho}(u,v) := (u, \mathsf{c}(1-u)v)$. The G^1 constraints between sectors and $\bar{C}^1$ constraints between top and bottom patches are enforced by setting

$$\acute{\mathbf{p}}_{01} := -\grave{\mathbf{p}}_{01} + 2(1-\mathsf{c})\grave{\mathbf{p}}_{00} + 2\mathsf{c}\grave{\mathbf{p}}_{10}; \tag{17}$$

$$\grave{\mathbf{p}}_{20} := \frac{\mathsf{c}\grave{\mathbf{p}}_{00} + 3(\mathsf{c}-2)\grave{\mathbf{p}}_{10} + 3(\grave{\mathbf{p}}_{11} + \acute{\mathbf{p}}_{11})}{4\mathsf{c}}; \tag{18}$$

$$\grave{\mathbf{p}}_{30} := -\frac{1}{4}\grave{\mathbf{p}}_{10} + \grave{\mathbf{p}}_{20} + \frac{1}{4}\underline{\grave{\mathbf{p}}}_{20}; \tag{19}$$

$$\acute{\mathbf{p}}_{21} := -\grave{\mathbf{p}}_{21} - \frac{2\mathsf{c}}{3}\grave{\mathbf{p}}_{10} + 2\grave{\mathbf{p}}_{20} + \frac{2\mathsf{c}}{3}\grave{\mathbf{p}}_{30}; \tag{20}$$

$$\acute{\mathbf{p}}_{31} := -\grave{\mathbf{p}}_{31} - \mathsf{c}\grave{\mathbf{p}}_{20} + (2+\mathsf{c})\grave{\mathbf{p}}_{30}; \tag{21}$$

$$\underline{\grave{\mathbf{p}}}_{20} := \frac{3(\underline{\grave{\mathbf{p}}}_{21} + \underline{\acute{\mathbf{p}}}_{21}) - \mathsf{c}\underline{\grave{\mathbf{p}}}_{30}}{6-\mathsf{c}}; \tag{22}$$

$$\underline{\grave{\mathbf{p}}}_{30} := \frac{1}{2}\underline{\grave{\mathbf{p}}}_{31} + \frac{1}{2}\underline{\acute{\mathbf{p}}}_{31}. \tag{23}$$

Splitting each sector's bi-4 patch into 2 × 2 by de Casteljau's algorithm, the operator $H^{\square}$ is applied to all domain corners of the four subpatches, see Fig. 10 : for a sub-patch $f : (u,v) \to \mathbb{R}^3$, the Hermite data $\begin{pmatrix} f & \partial_u f \\ \partial_v f & \partial_u\partial_v f\end{pmatrix}$ is transformed to 2 × 2 nets (cyan and blue) of BB-coefficients of degree bi-3 and these are merged to form a bi-3 patch. By construction the six ○ BB-coefficients of adjacent sectors (see Fig. 9 b,bottom and Fig. 9 a) satisfy (22) and (23).

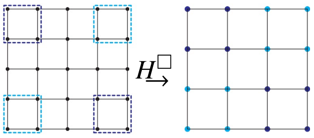

Figure 10: Bi-4 to bi-3 transformation $H^\square$.

We apply the approach of (16) to set $\mathbf{p}^{s,\mathbf{c}}_{3,1}$ (□ in Fig. 9 a) and $\mathbf{p}^{s,\mathbf{c}}_{3,0}$ (marked □) to enforce (18) and (19) and set

$$\mathbf{p}^{s,\triangleright}_{3,3} := \mathbf{p}^{s,\mathbf{c}}_{3,0}, \quad \mathbf{p}^{s,\triangleright}_{3,2} := 2\mathbf{p}^{s,\mathbf{c}}_{3,0} - \mathbf{p}^{s,\mathbf{c}}_{3,0}.$$

Then (20) and (21) hold due to

$$\grave{\mathbf{a}}_{21} := \tilde{\mathbf{p}}^{s,\mathbf{c}}_{21},\ \acute{\mathbf{a}}_{21} := \tilde{\mathbf{p}}^{s+1,\mathbf{c}}_{1,2}, \breve{\mathbf{p}}_2 := -\frac{2\mathsf{c}}{3}\grave{\mathbf{p}}_{10} + 2\grave{\mathbf{p}}_{20} + \frac{2\mathsf{c}}{3}\grave{\mathbf{p}}_{30};$$
$$\grave{\mathbf{a}}_{31} := \tilde{\mathbf{p}}^{s,\mathbf{c}}_{20},\ \acute{\mathbf{a}}_{31} := \tilde{\mathbf{p}}^{s+1,\mathbf{c}}_{02}, \breve{\mathbf{p}}_3 := -\mathsf{c}\grave{\mathbf{p}}_{20} + (2+\mathsf{c})\grave{\mathbf{p}}_{30},$$

where $\tilde{\mathbf{p}}^{s,\mathbf{c}}_{i,j}$, $\tilde{\mathbf{p}}^{s,\mathbf{c}}_{i,j}$ are the BB-coefficients of bi-3 patches after split followed by $H^\square$. The BB-coefficients ○ of patches $\mathbf{p}^{s,\triangleright}_{2,2}$ and $\mathbf{p}^{s+1,\triangleleft}_{2,2}$ are defined by C^1 extension.

We observe that the bi-4-to-bi-3 conversion process above preserves the C^1 join of neighboring MSV scaffold patches. This proves overall smoothness. The algorithm can be run symbolically to obtain the weights of all BB-coefficients of one 2 × 2 sector (sufficient due to symmetry) in terms of the CC-net for an implementation as matrix multiplication.

3.2. *Single bi-3 patch per sector*

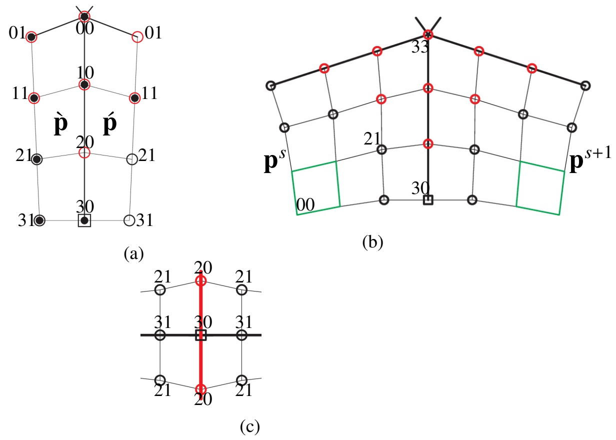

(a) (b) (c)

Figure 11: Single sector: (a) the choice of free BB-coefficients (•) for G^1 constraints between sectors; (b) the adjacent sector patches. The BB-coefficients in (a) and (b) are related by $\grave{\mathbf{p}}_{ij} := \mathbf{p}^s_{3-j,3-i}$, $\acute{\mathbf{p}}_{ij} := \mathbf{p}^{s+1}_{3-i,3-j}$. (c) Local correction to ensure a C^1 join.

For a single patch per sector, the G^1 constraints, with the reparameterization $\rho(u,v)$ of (1), are enforced by setting, see Fig. 11,

$$\acute{\mathbf{p}}_{01} := -\grave{\mathbf{p}}_{01} + 2(1-\mathsf{c})\grave{\mathbf{p}}_{00} + 2\mathsf{c}\grave{\mathbf{p}}_{10}; \tag{24}$$

$$\grave{\mathbf{p}}_{20} := \frac{1}{4\mathsf{c}}\Big(3(\grave{\mathbf{p}}_{11} + \acute{\mathbf{p}}_{11}) + (4\mathsf{c}-6)\grave{\mathbf{p}}_{10}\Big); \tag{25}$$

$$\acute{\mathbf{p}}_{21} := -\grave{\mathbf{p}}_{21} + 2\grave{\mathbf{p}}_{20} + \frac{2\mathsf{c}}{3}(\grave{\mathbf{p}}_{30} - \grave{\mathbf{p}}_{20}); \tag{26}$$

$$\acute{\mathbf{p}}_{31} := 2\grave{\mathbf{p}}_{30} - \grave{\mathbf{p}}_{31}. \tag{27}$$

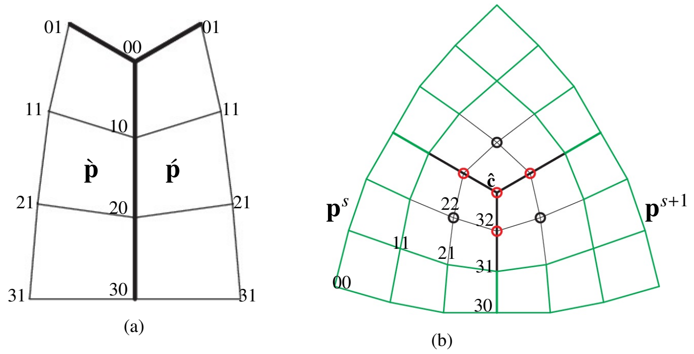

Figure 12: $n = 3$, single sector: (a) BB-coefficients marked • are unconstrained after enforcing the G^1 constraints between two sectors; (b) all patches.

Applying $H^\square$ at the four corners of the auxiliary bi-4 patch of the sector yields an initial bi-3 patch $\tilde{\mathbf{p}}^s$. We retain the 2 × 2 BB-subnet containing $\hat{\mathbf{c}}$, i.e. $\mathbf{p}^s_{ij} := \tilde{\mathbf{p}}^s_{ij}$, $i = 2,3$, $j = 2,3$ and $\mathbf{p}^s_{ij} := \tilde{\mathbf{p}}^s_{ij}$ for $i = 0,1$, $j = 0,1$ (green BB-subnet in Fig. 11 b). The latter do not affect the G^1 join between sectors and are consistent with a C^1 join to neighboring caps: the boundary of $\mathbf{p}^s$ and green BB-subnet coincide with the tensor-border $\mathbf{t}^s$ so that $\tilde{\mathbf{p}}^s_{20} := \mathbf{t}^s_{20}$ and

$$\tilde{\mathbf{p}}^s_{21} := \frac{1}{3(2-\mathsf{c})}\Big(3(2\mathbf{t}^s_{21} - \mathsf{c}\mathbf{t}^s_{20}) - 2\mathsf{c}(\mathbf{t}^s_{31} - \mathbf{t}^s_{30})\Big),$$

see Fig. 11 c. However enforcing (25) implies that (26) and the C^1 join to the neighboring bi-3 cap no longer hold: the BB-coefficient shown as □ with label 30 in Fig. 11 a needs to be the average of its two neighbors ○ labeled 20 and the BB-coefficients with labels 21 respectively 31 in Fig. 11 c need to be updated according to (16):

$$\grave{\mathbf{a}}_{21} := \tilde{\mathbf{p}}^s_{21},\ \acute{\mathbf{a}}_{21} := \tilde{\mathbf{p}}^{s+1}_{12},\ \breve{\mathbf{p}}_2 := 2\grave{\mathbf{p}}_{20} + \frac{2\mathsf{c}}{3}(\grave{\mathbf{p}}_{30} - \grave{\mathbf{p}}_{20}); \tag{28}$$

$$\grave{\mathbf{a}}_{31} := \tilde{\mathbf{p}}^s_{20},\ \acute{\mathbf{a}}_{31} := \tilde{\mathbf{p}}^{s+1}_{02},\ \breve{\mathbf{p}}_3 := 2\grave{\mathbf{p}}_{30}. \tag{29}$$

The remaining coefficients $\mathbf{p}^s_{22}$ and $\mathbf{p}^s_{32}$ are given in Appendix 2, based on symbolic execution of the algorithm that guarantees exact smoothness of the surface (before the careful truncation of weights).

3.3. *Valence $n = 3$ (sphere-like surfaces)*

According to [2], the number of irregular nodes in an MSV mesh of valence n is $\frac{8(1-g)}{4-n}$. Since the number of nodes must be positive, when $n = 3$ the topological genus must be $g = 0$. That is, the topology is sphere-like. For $n = 3$, the G^1 constraints for single patch bi-3 sectors can be enforced by setting

$$\acute{\mathbf{p}}_{01} := -\grave{\mathbf{p}}_{01} + 2(1-\mathsf{c})\grave{\mathbf{p}}_{00} + 2\mathsf{c}\grave{\mathbf{p}}_{10}; \tag{30}$$

$$\acute{\mathbf{p}}_{11} := -\grave{\mathbf{p}}_{11} + 2\grave{\mathbf{p}}_{10} + \frac{4\mathsf{c}}{3}(\grave{\mathbf{p}}_{20} - \grave{\mathbf{p}}_{10}); \tag{31}$$

$$\grave{\mathbf{p}}_{20} := \frac{1}{2(3-\mathsf{c})}\Big(3(\grave{\mathbf{p}}_{21} + \acute{\mathbf{p}}_{21}) - 2\mathsf{c}\grave{\mathbf{p}}_{30}\Big); \tag{32}$$

$$\grave{\mathbf{p}}_{30} := \frac{1}{2}\grave{\mathbf{p}}_{31} + \frac{1}{2}\acute{\mathbf{p}}_{31}. \tag{33}$$

Initializing bi-3 patches $\tilde{\mathbf{p}}^s$ as in Section 3.2 yields C^1 joined multi-sided caps and only (31) does not hold. The three linear equations (31) have the unique solution

$$\mathbf{p}^s_{22} := \frac{4}{3}(\mathbf{p}^s_{32} - \mathbf{p}^{s+1}_{32} + \mathbf{p}^{s+2}_{32}) - \frac{1}{3}(\mathbf{p}^s_{31} - \mathbf{p}^{s+1}_{31} + \mathbf{p}^{s+2}_{31}).$$

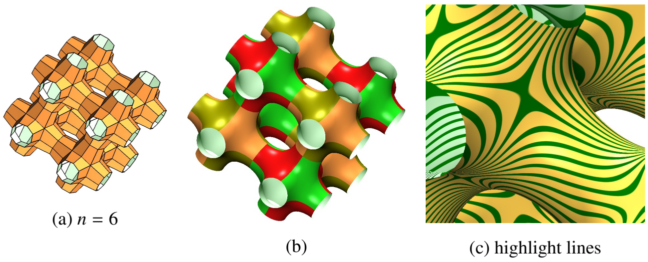
(a) $n = 6$ (b) (c) highlight lines

Figure 13: Classic 3D grid

We adjust the formulas from Appendix 2 for $n = 3$ so that $\hat{\mathbf{c}} = \frac{1}{3}(\mathbf{p}^0_{32} + \mathbf{p}^1_{32} + \mathbf{p}^2_{32})$ yielding a well-defined tangent plane at $\hat{\mathbf{c}}$. Then

$$\mathbf{p}^s_{32} := (1 - \sum_{r=0}^{2}\sum_{k=1}^{6} \ddot{a}^r_k)\,\mathbf{c}_0 + \sum_{r=0}^{2}\sum_{k=1}^{6} \ddot{a}^r_k \mathbf{c}^{s+r}_k \tag{34}$$

$$(\ddot{a}^{r=0,1,2}_{k=1,\dots,6}) := \frac{1}{3}\frac{1}{10^5}\begin{pmatrix} 82 & 295 & 1410 & 37 & 23092 & 83876 \\ 82 & 37 & -705 & 295 & 23092 & 33062 \\ -164 & -332 & -705 & -332 & 691 & 33062 \end{pmatrix}.$$

The C^1 join of the bi-3 G^1 caps follows by setting

$$\mathbf{p}^s_{i0} := \mathbf{t}^s_{i0}, i = 0, \dots, 3; \quad \mathbf{p}^s_{i1} := \mathbf{t}^s_{i1},\ i = 0, 1;$$
$$\mathbf{p}^s_{21} := \frac{1}{5}(\mathbf{t}^s_{20} + 4\mathbf{t}^s_{21}) - \frac{2}{15}(\mathbf{t}^s_{30} - \mathbf{t}^s_{31}), \quad \mathbf{p}^s_{31} := \frac{1}{5}(\mathbf{t}^s_{30} + 4\mathbf{t}^s_{31}).$$

Remark. The system of n linear equations has a unique solution of all odd n, but the shape is good only for $n = 3$.

4. Examples and comparisons

Minimal single-valence nets in nature or CAD design often represent an underlying graph embedded in $\mathbb{R}^3$ whose edges are offset to form quad faceted beams. We note that the number of irregular nodes of valence n in such an MSV net of genus g equals $\frac{8(1-g)}{4-n}$ (see [2]).

For graph embeddings that are not too distorted, the bi-3 MSV scaffold surfaces are visually indistinguishable from the considerably more complex G^2 surfaces [2].

For the most common regular 3D grid Fig. 13 a, already the single patch per sector construction yields a smooth highlight line distribution Fig. 13 c. Fig. 13 b shows the individual 6-sided caps built from 6 bi-3 patches each.

Since 2×2 bi-3 caps closely follow and are typically visually indistinguishable from their bi-4 antecedents, we display only bi-3 surfaces in this section. That does not mean that the auxiliary caps are not needed. The auxiliary caps are critical to provide the shape for difficult scaffolds such as Fig. 14 b and c.

The 2×2 cap construction yields good highlight line distributions even for extreme MSV nets, handcrafted to challenge the algorithm. Extreme nets do, however, reveal shortcomings of the single patch per sector construction. Fig. 15 features two surfaces of the same genus 2 with (a) $n = 5$ (eight irregular nodes) and (c) $n = 6$ (four irregular nodes). The difference between single and 2×2 is minimal for the net in (a) so that we only display single. By contrast, the scaffold surfaces of net (c) exhibit strong differences pointed to by the ↑ in (d) and (e): in (d) the surface folds back into the open interior but not in (e). This can be attributed to (a) using $8 * 5 = 40$ quads compared to (c) $4 * 6 = 24$ to capture the shape. The single patch constructions appear stiff.

In Fig. 16 single and 2×2 patch constructions look very similar and it requires a strong twisting to bring out the differences due to flexibility, see ↑.

Due to the strong interaction of nearby nodes scaffold surfaces strongly smooth out their control net akin to C^{k-1} splines of high degree k. The scaffold surface based on Fig. 17 a shows less oscillation when using 2×2 patches. Fig. 17 f adds spikes to the Möbius strip (whose non-orientability is indicated by the flip of the spike to the right). The scaffold surfaces show much milder protrusions than the spikes. The differences between the stiffer single (g) and the rounder 2×2 construction (h) are visible in magnification. Fig. 18 makes the same point for a double twist, illustrating that the scaffold determines the complexity of the shape. Both shapes are inspired by the structure of DNA.

Fig. 19 explores alternative approaches to creating single bi-3 default caps in Section 3.2. Since the default replaces much of its auxiliary bi-4 input, it is natural to ask whether a 'direct, local' construction is possible by setting the 5 unconstrained coefficients of the quadratic $\mathbf{q}$ at $\hat{\mathbf{c}}$ (○ in Fig. 11) to minimize a functional $\mathcal{F}_k$ and then applying the G^1 adjustment (28) and the C^1 join of adjacent caps as in Section 3.2. Fig. 19 a shows that $\mathcal{F}_4$ yields an unacceptably creased result, $\mathcal{F}_2$ and $\mathcal{F}_3$ fare worse and are not shown. Direct local construction using $\mathcal{F}_5$ and $\mathcal{F}_6$ (b) and (c) looks increasingly better but still far worse than the default shown in Fig. 11 g,h. (Higher choices of k in $\mathcal{F}_k$ yield 0 for bi-cubic patches.) Next we tried a 'direct, global' construction, where we substitute in the G^1 adjustment (28) and the C^1 join of adjacent caps and solve for all $5m$ terms of quadratics of the m caps in the scaffold at the same time, i.e. solving the $5m \times 5m$ linear system of equations. The corresponding surfaces, denoted as $\mathcal{F}^g_k$ in Fig. 19 , are still worse than the default: $\mathcal{F}^g_6$ yields the best result, but its highlight lines oscillating more than the default.

The MSV net of Fig. 20 has an icosahedral structure. The outcomes confirm that, for MSV nets derived by inflating the edges of a graph, the visual difference between single and 2×2 is typically negligible. And even though the BB-net in Fig. 20 b has high variation, the highlight lines of the single patch scaffold in Fig. 20 c are uniformly distributed.

Fig. 21 shows design where top and bottom are joined by (a) 3 tubes, (e) 4 tubes and (h) 12 tubes. Although both highlight line distributions in (c) and (d) are acceptable, the 2×2 distribution is clearly more uniform. The top views in (f) and (g) and the side view of (i) vs (j) show an undesirable flaring-out of the single patch construction. Remarkably, even though inputs like Fig. 16 d and Fig. 21 h are extreme, the 2×2 cap has acceptable shape.

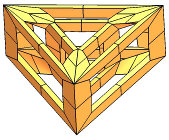
(a) $n = 8$, genus 13

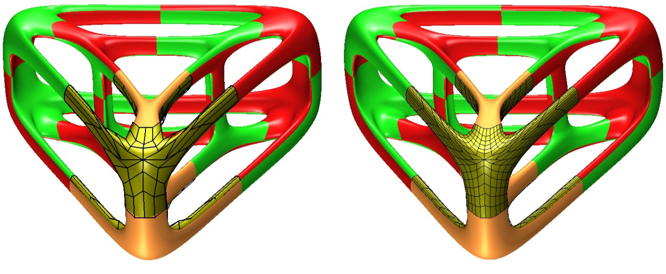
(b) single (c) 2×2

Figure 14: High genus MSV net. (b) single bi-3 patch per quad, (c) 2×2 bi-3 patches per quad.

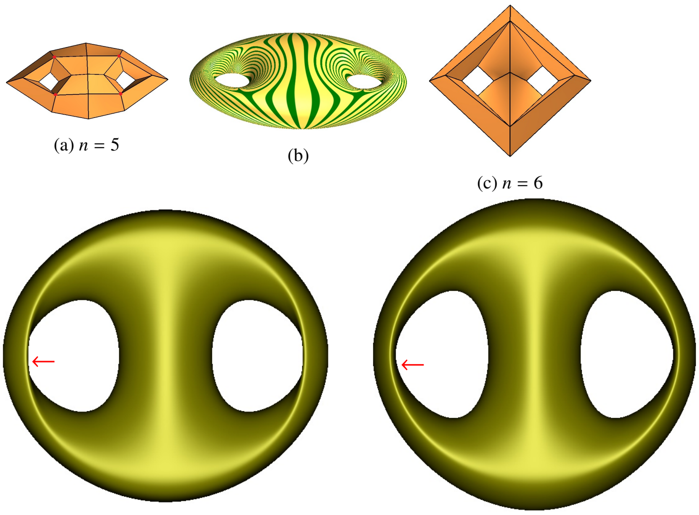
(a) $n = 5$ (b) (c) $n = 6$

(d) single (e) 2×2

Figure 15: MSV net, genus 2: (a) 8 irregular nodes of valence 5 marked as •; (b) corresponding surface. (c) 4 irregular nodes of valence 6 yielding (d,e). The ← points to where the single patch surface folds inwards while the 2×2 surface looks relaxed.

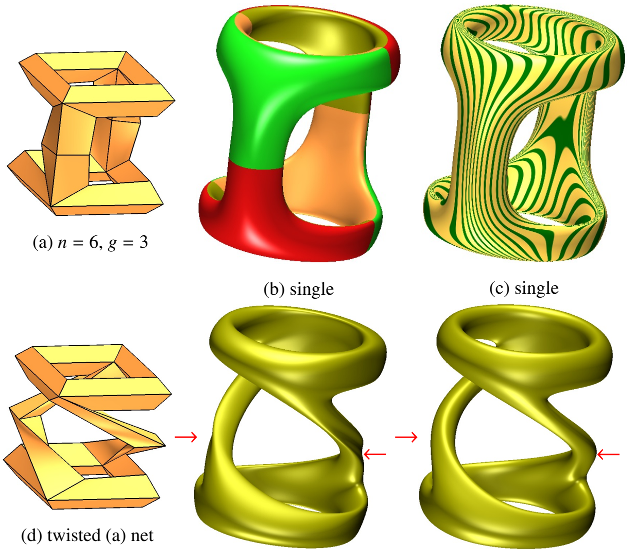
(a) $n = 6$, $g = 3$ (b) single (c) single

(d) twisted (a) net (e) single (f) 2×2

Figure 16: MSV mesh, genus 3. (b) surface caps (c) highlight lines. (d) Twisting the mesh leads to more creased geometry for the single patch construction compared to 2×2, see ←.

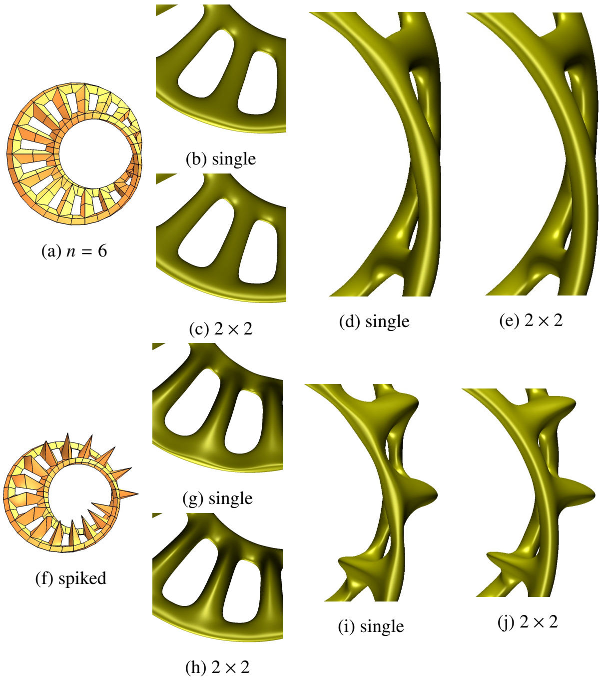
(a) $n = 6$ (b) single (c) 2×2 (d) single (e) 2×2

(f) spiked (g) single (h) 2×2 (i) single (j) 2×2

Figure 17: Möbius nets.

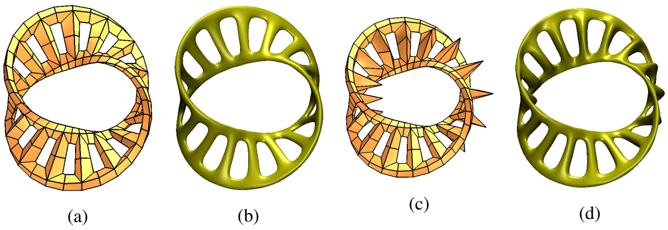
(a) (b) (c) (d)

Figure 18: Double twisted net.

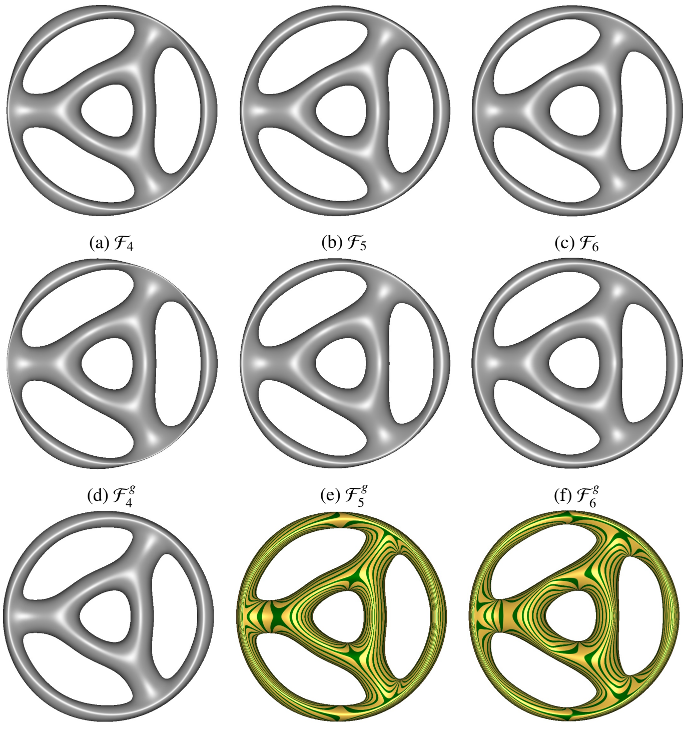
(a) $\mathcal{F}_4$ (b) $\mathcal{F}_5$ (c) $\mathcal{F}_6$
(d) $\mathcal{F}_4^g$ (e) $\mathcal{F}_5^g$ (f) $\mathcal{F}_6^g$
(g) single (default) (h) single (default) (i) $\mathcal{F}_6^g$

Figure 19: Comparing the single bi-3 default scaffold surface with alternative single bi-3 constructions via functionals $\mathcal{F}_k$.

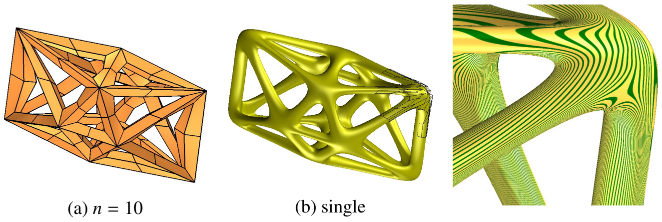
(a) $n = 10$ (b) single (c)

Figure 20: Icosahedral net. (c) highlight line distribution near the joint.

Since the number of irregular nodes in an MSV mesh of valence n is $\frac{8(1-g)}{4-n}$, $n = 3$ implies sphere-like genus $g = 0$ and 8 irregular nodes. That is, any $n = 3$ MSV net has the structure of a once-refined cube, see Fig. 22 a. The highlight line distributions are good until the shape is extremely twisted in Fig. 22 g. The single patch algorithm strongly smoothes out distortions but close scrutiny of Fig. 22 i reveals that, as we knew, the surfaces are G^1, not G^2.

5. Discussion and Conclusion

Minimal single-valence (MSV) meshes are ubiquitous as quad offsets from graphs with repeating patterns. Such graphs arise both in design and in nature. While, structurally, MSV meshes are as restrictive for free-form design as are regular quad meshes, large repetitive arrangements of MSV themes in design and nature can form complex macro shapes as illustrated in Fig. 2 and Fig. 17 vs Fig. 18 . The dual graph of any triangulation (periodic to form a cylinder or non-periodic) can be offset to yield an $n = 6$ MSV mesh, see Fig. 2 . The dual graph of any quad mesh, can be offset to yield an $n = 8$ MSV mesh (see Fig. 23 , Fig. 24) or, requiring 4 times as many nodes, a valence $n = 5$ MSV mesh.

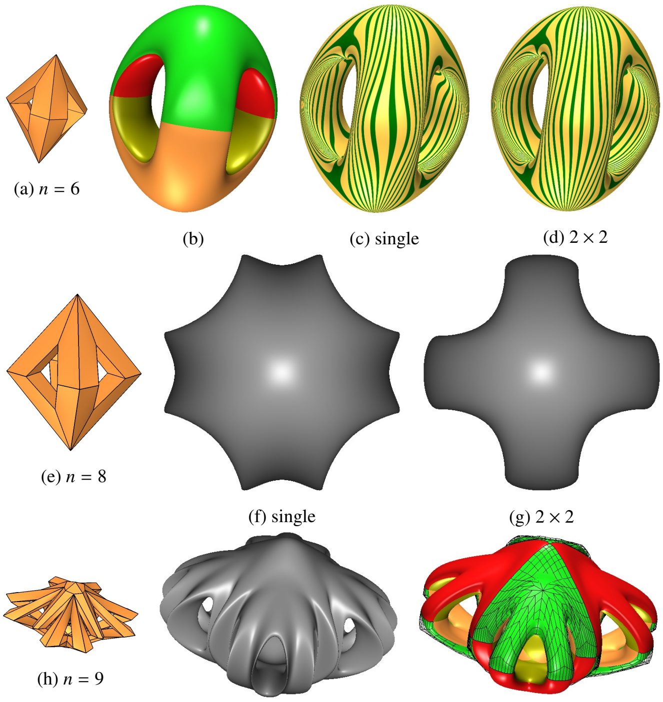
(a) $n = 6$ (b) (c) single (d) 2×2
(e) $n = 8$ (f) single (g) 2×2
(h) $n = 9$ (i) single (j) 2×2

Figure 21: Variants of MSV cages. (a) $n = 6$, 4 irregular nodes, (e) $n = 8$, 4 irregular nodes, (h) $n = 9$, 16 irregular nodes.

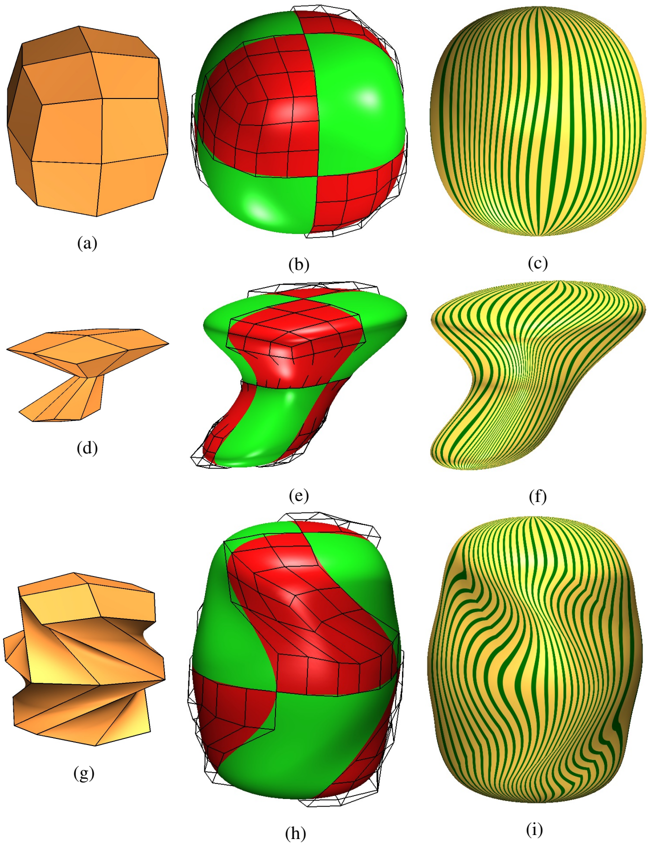
(a) (b) (c)
(d) (e) (f)
(g) (h) (i)

Figure 22: $n = 3$, surfaces with the single sector. (a,d,g): MSV nets. (b,e,h): caps, some with their BB-nets. (c,f,i): highlight lines.

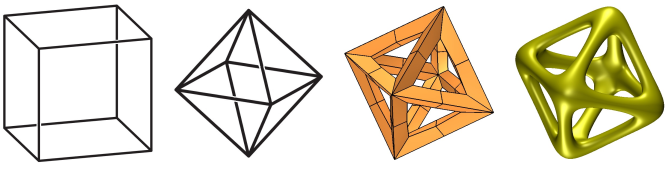

(a) quad mesh (b) dual (c) quad-offset (d) surface

Figure 24: Quad mesh, its dual, offset and $n = 8$ MSV surface.

One or more subdivision steps can be applied to a polyhdral mesh to generate a quad mesh, or its dual. Moreover, any 3D-graph can have its m-valent vertices replaced by an m-gon. Truncation of the edges meeting at the vertex and joining the new vertices to their truncation neighbors in order, generates graphs with vertices of valence 3. This is illustrated in Fig. 25 for a tetrahedron where the single patch construction is sharper-featured than 2×2, but both options yield good results for the truncated tetrahedron.

This paper introduced two highly efficient options for smoothing out MSV meshes and provide a smooth bi-cubic scaffold surface. Here *efficient* has a three-fold meaning: low degree (bi-cubic), low number of pieces (as low as one piece per sector, hence n pieces per cap and a total of $\frac{8n(1-g)}{4-n}$ patches for the whole surface), and explicit formulas that pre-solve the underlying equations and present them with necessary and sufficient accuracy for good visual display.

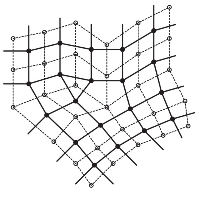

Figure 23: The dual (solid) of a quad mesh (dashed).

From the examples and comparisons of the previous section, the reader can glean the trade off when choosing between the 2×2 patch option (typically visually indistinguishable for the auxiliary bi-4 patch) whose highlight line uniformity is robust against large deformations, and the single bi-3 option that is optimally succinct but can be too stiff for highly twisted configurations. Fig. 3 compares the single option to an older bi-3 C^1 technique. The bi-3 construction in [26] yields good shape but is not C^1 and uses more pieces. Asymmetric higher-order saddles in MSV surfaces lead to well-known shape artifacts when using Catmull-Clark subdivision surfaces [15]. Bi-2 constructions can suffer from kinks in the high-light lines already in the regular tensor-product part of a surface and so are out of consideration.

The auxiliary bi-4 can serve as a final cap (with formulas provided in Appendix 1) if the number of patches needs to be kept low and the shape robust against large deformations. Modern bi-4 G^1 surface constructions yield surfaces akin to the auxiliary bi-4 construction presented in Section 4, but use more complex algorithms. Bi-4 is higher degree than wanted, considering that the scaffolds can be very large. Besides, if degree bi-4 were acceptable then, at the cost of more pieces, [2] could be applied.

Since G-splines are directly suitable for isogeometric analysis [23], especially for unstructured layouts [22, 3, 24, 25], the new bi-3 scaffold surfaces will yield additional tools for analyzing truss and micro-structures.

References

[1] K.-P. Beier, Y. Chen, Highlight-line algorithm for realtime surface-quality assessment, Comp-Aid Design 26 (4) (1994) 268–277.

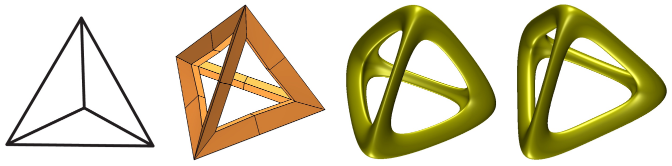

(a) graph (b) quad offset (c) single (d) 2×2

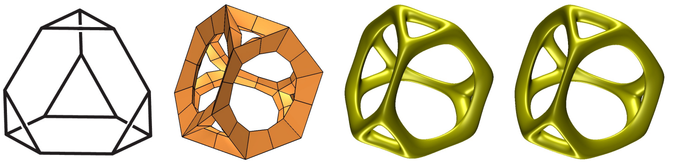

(e) truncated (f) quad offset (g) single (h) 2×2

Figure 25: Truncation of the tetrahedron yields another $n = 6$ MSV mesh.

[2] K. Karčiauskas, J. Peters, Curvature continuous bi-4 constructions for scaffold- and sphere-like surfaces, Computer Aided Design (SPM 2016) 78 (2016) 48–59.

[3] A. Collin, G. Sangalli, T. Takacs, Analysis-suitable G^1 multi-patch parametrizations for C^1 isogeometric spaces, Computer Aided Geometric Design 47 (2016) 93–113.

[4] J. Fan, J. Peters, Smooth bi-3 spline surfaces with fewest knots, Computer Aided Design 43 (2) (2011) 180–187, jCAD 1686.

[5] J. A. Bærentzen, R. Abdrashitov, K. Singh, Interactive shape modeling using a skeleton-mesh co-representation, ACM Transactions on Graphics (TOG) 33 (4) (2014) 1–10.

[6] F. Usai, M. Livesu, E. Puppo, M. Tarini, R. Scateni, Extraction of the quad layout of a triangle mesh guided by its curve skeleton, ACM Transactions on Graphics (TOG) 35 (1) (2015) 1–13.

[7] A. J. F. Suárez, E. Hubert, Scaffolding skeletons using spherical voronoi diagrams: Feasibility, regularity and symmetry, Comput. Aided Des 102 (2018) 83–93.

[8] A. Panotopoulou, E. Ross, K. Welker, E. Hubert, G. Morin, Scaffolding a skeleton, in: Research in Shape Analysis, Springer, 2018, pp. 17–35.

[9] J. Peters, Splines for meshes with irregularities, The SMAI journal of computational mathematics S5 (2019) 161–183.

[10] T. Várady, P. Salvi, A. P. Rockwood, Transfinite surface interpolation with interior control, Graph. Model 74 (6) (2012) 311–320.

[11] P. Salvi, T. Várady, A. P. Rockwood, Ribbon-based transfinite surfaces, Comput. Aided Geom. Des 31 (9) (2014) 613–630.

[12] P. Salvi, T. Várady, Multi-sided Bézier surfaces over concave polygonal domains, Comput. Graph 74 (2018) 56–65.

[13] G. J. Hettinga, J. Kosinka, Multisided B-spline Patches Over Extraordinary Regions, in: S. Biasotti, R. Pintus, S. Berretti (Eds.), Smart Tools and Apps for Graphics - Eurographics Italian Chapter Conference, The Eurographics Association, 2020.

[14] G. J. Hettinga, J. Kosinka, A multisided C^2 B-spline patch over extraordinary vertices in quadrilateral meshes, Comput. Aided Des 127 (2020) 102855.

[15] E. Catmull, J. Clark, Recursively generated B-spline surfaces on arbitrary topological meshes, Computer-Aided Design 10 (1978) 350–355.

[16] X. Wei, Y. J. Zhang, D. Toshniwal, H. Speleers, X. Li, C. Manni, J. A. Evans, T. J. Hughes, Blended b-spline construction on unstructured quadrilateral and hexahedral meshes with optimal convergence rates in isogeometric analysis, Computer Methods in Applied Mechanics and Engineering 341 (C).

[17] J. Gregory, J. Hahn, Geometric continuity and convex combination patches, Computer Aided Geometric Design 4 (1-2) (1987) 79–89.

[18] C. T. Loop, S. Schaefer, G^2 tensor product splines over extraordinary vertices, Comput. Graph. Forum 27 (5) (2008) 1373–1382.

[19] G.-P. Bonneau, S. Hahmann, Flexible G^1 interpolation of quad meshes, Graphical Models 76 (6) (2014) 669–681.

[20] M. Kapl, G. Sangalli, T. Takacs, Dimension and basis construction for analysis-suitable g^1 two-patch parameterizations, Computer Aided Geometric Design 52-53 (2017) 75–89.

[21] A. Blidia, B. Mourrain, N. Villamizar, G^1-smooth splines on quad meshes with 4-split macro-patch elements, Comput. Aided Geom. Des. 52 (2017) 106–125.

[22] D. Groisser, J. Peters, Matched G^k-constructions always yield C^k-

continuous isogeometric elements, Computer Aided Geometric Design 34 (2015) 67–72.

[23] T. J. R. Hughes, J. A. Cottrell, Y. Bazilevs, Isogeometric analysis: Cad, finite elements, NURBS, exact geometry and mesh refinement, CMAME 194 (39-41) (2005) 4135–4195.

[24] M. Kapl, F. Buchegger, M. Bercovier, B. Jüttler, Isogeometric analysis with geometrically continuous functions on planar multi-patch geometries, Computer Methods in Applied Mechanics and Engineering 316 (2017) 209–234.

[25] T. Nguyen, K. Karčiauskas, J. Peters, A comparative study of several classical, discrete differential and isogeometric methods for solving Poisson's equation on the disk, Axioms 3 (2) (2014) 280–299.

[26] K. Karčiauskas, J. Peters, Can bi-cubic surfaces be class A?, Computer Graphics Forum 34 (5) (2015) 229–238.

[27] M. A. Sabin, C. Fellows, J. Kosinka, CAD model details via curved knot lines and truncated powers, Comput. Aided Des. 143 (2022) 103137.

[28] C. de Boor, B-form basics, in: G. Farin (Ed.), Geometric Modeling: Algorithms and New Trends, SIAM, 1987, pp. 131–148.

[29] G. Farin, Curves and Surfaces for Computer Aided Geometric Design: A Practical Guide, Academic Press, 1988.

[30] T. D. DeRose, Necessary and sufficient conditions for tangent plane continuity of Bézier surfaces, Comp Aid Geom Design 7 (1) (1990) 165–179.

[31] M. Halstead, M. Kass, T. DeRose, Efficient, fair interpolation using catmull-clark surfaces, in: L. Valastyan, L. Walsh (Eds.), Proceedings of the 20th annual conference on Computer graphics and interactive techniques, Siggraph 1993, ACM Press, New York, NY, USA, 1993, pp. 35–44.

Appendix 1: Explicit formulas for the bi-4 cap

Due to symmetry, it suffices to compute $\mathbf{p}^s_{33}$ and $\mathbf{p}^s_{43}$ for $s = 0$ from the nodes of CC-net. Then for any sector $s = 0, \dots, n-1$,

$$\mathbf{p}^s_{33} := \dot a_0 \mathbf{c}_0 + \sum_{r=0}^{n-1} \sum_{k=1}^{6} \dot a^r_k \mathbf{c}^{s+r}_k; \ \mathbf{p}^s_{43} := \ddot a_0 \mathbf{c}_0 + \sum_{r=0}^{n-1} \sum_{k=1}^{6} \ddot a^r_k \mathbf{c}^{s+r}_k, \quad (35)$$

where $\dot a_0 := 1 - \sum_{r=0}^{n-1} \sum_{k=1}^{6} \dot a^r_k$, $\ddot a_0 := 1 - \sum_{r=0}^{n-1} \sum_{k=1}^{6} \ddot a^r_k$. and $\dot a^r_k$ and $\ddot a^r_k$ obey the symmetry relations:

$$\dot a^s_2 = \dot a^{-s}_4,\ \dot a^s_4 = \dot a^{-s}_2, \dot a^s_5 = \dot a^{-s}_5, \dot a^s_3 = \dot a^{-s-1}_3,\ \dot a^s_6 = \dot a^{-s-1}_6;$$
$$\ddot a^s_2 = \ddot a^{-s+1}_4,\ \ddot a^s_4 = \ddot a^{-s+1}_2, \ddot a^s_5 = \ddot a^{-s+1}_5, \ddot a^s_3 = \ddot a^{-s}_3, \ddot a^s_6 = \ddot a^{-s}_6.$$

By Appendix 3, the weights $\dot a^r_k$ and $\ddot a^r_k$ can be truncated to 5 digits after the decimal point so that it suffices to define the following $\dot a$ and $\ddot a$ (scaled by 10^5 for easy readability, i.e. for $n = 5$, $\dot a^1_5 = 0.02129$ and for $n = 7$, $\ddot a^1_5 = .02836$). We abbreviate $N := \lfloor \frac{n}{2} \rfloor$, i.e. $N = 3$ for $n \in \{6, 7\}$ and $M := \lfloor \frac{n+1}{2} \rfloor$, i.e. $M = 4$ for $n \in \{7, 8\}$.

n	$10^5\times$	$\dot a^{r=0,\dots,N}_{k=1,\dots,6}$	$\ddot a^{r=1,\dots,M}_{k=1,2,4,5}$	$\ddot a^{r=0,\dots,N}_{k=3,6}$
5		39 −225 −443 −225 7600 18847 0 5 239 2 2129 1737 −18 39 242 104 −303 859	14 −77 −66 3999 −5 18 36 1236 −18 89 89 −471	−291 15504 −90 10318 235 1929
6		29 −306 −788 −306 6654 17819 7 −64 169 −84 2757 2858 −13 86 388 134 −565 −508 −12 63 388 63 6 −508	11 −103 −98 3328 0 −5 5 1515 −11 98 103 −297	−428 12725 −214 9392 214 2728 428 −603
7		21 −341 −1015 −341 5861 16583 9 −126 −27 −161 3092 4345 −7 88 460 106 −339 −1299 −10 75 412 104 −303 −379	8 −115 −114 2836 2 −28 −27 1596 −5 79 79 51 −9 127 127 −636	−496 10693 −309 8460 110 3442 447 −582
8		16 −353 −1149 −353 5231 15335 9 −171 −240 −214 3214 5573 −3 61 425 52 82 −1169 −8 98 458 127 −593 −944 −7 79 458 79 −153 −944	6 −119 −121 2463 2 −47 −52 1583 −2 52 47 339 −6 121 119 −540	−525 9165 −371 7607 0 3846 371 84 525 −1472
9		13 −355 −1218 −355 4719 14167 8 −202 −423 −248 3213 6421 0 23 316 −4 504 −468 −5 106 490 123 −654 −1547 −6 81 436 98 −306 −690	5 −120 −123 2170 2 −60 −69 1526 −1 27 17 539 −4 102 96 −328 −5 130 130 −671	−531 7985 −407 6859 −92 4009 265 769 499 −1345
10		11 −349 −1243 −349 4294 13109 7 −222 −565 −266 3144 6937 1 −14 176 −52 854 431 −3 98 478 99 −538 −1772 −5 92 445 113 −500 −983 −6 79 445 79 −212 −983	4 −119 −122 1935 2 −70 −79 1450 0 5 −5 666 −2 79 70 −117 −4 122 119 −601	−525 7052 −425 6214 −162 4021 162 1311 425 −881 525 −1718

Appendix 2: Explicit formulas for the bi-3 single patch cap

Replacing in the expression of Appendix 1 $\mathbf{p}^s_{44}$ by $\mathbf{p}^s_{33}$, $\mathbf{p}^s_{33}$ by $\mathbf{p}^s_{22}$ and $\mathbf{p}^s_{43}$ by $\mathbf{p}^s_{32}$, the weights in the bi-3 case are ($N := \lfloor \frac{n}{2} \rfloor$, $M := \lfloor \frac{n+1}{2} \rfloor$):

n	$10^5\times$	$\dot a^{r=0,\dots,N}_{k=1,\dots,6}$	$\ddot a^{r=1,\dots,M}_{k=1,2,4,5}$	$\ddot a^{r=0,\dots,N}_{k=3,6}$
5		58 −336 −620 −336 10180 22919 −3 36 362 19 1681 −1465 −22 23 222 130 −657 702	20 −103 −89 4666 −8 25 48 982 −24 119 119 −1296	−389 18005 −120 11092 314 −95
6		42 −455 −1117 −455 9040 22522 8 −66 302 −108 2919 368 −19 112 406 191 −1379 −1174 −11 23 406 23 445 −1174	15 −138 −131 3932 0 −7 7 1515 −15 131 138 −902	−571 14947 −285 10504 285 1618 571 −2825
7		30 −504 −1447 −504 8031 21498 11 −162 39 −223 3660 2964 −12 136 571 166 −1204 −3052 −11 43 337 94 −147 372	11 −153 −153 3385 3 −38 −37 1732 −8 105 106 −328 −13 170 170 −1245	−662 12670 −413 9693 147 3002 596 −2363
8		23 −522 −1645 −522 7217 20237 12 −231 −263 −304 4023 5246 −6 107 591 95 −601 −3399 −10 97 417 153 −859 −634 −8 34 417 34 313 −634	9 −160 −163 2964 4 −63 −70 1791 −4 70 63 132 −9 163 160 −1041	−701 10938 −495 8861 0 3846 495 −1169 701 −3246
9		18 −523 −1748 −523 6549 18942 11 −280 −531 −355 4158 6937 −2 57 486 15 67 −2604 −8 131 532 168 −1168 −2143 −8 41 331 75 −13 321	7 −161 −165 2630 4 −81 −92 1771 −1 36 24 454 −6 137 129 −703 −8 173 173 −1160	−709 9589 −543 8088 −123 4288 355 −33 666 −2853
10		15 −514 −1788 −514 5988 17705 11 −312 −743 −384 4160 8079 1 3 314 −56 652 −1308 −6 137 589 149 −1127 −3046 −7 74 369 118 −497 −296 −6 34 369 34 232 −296	6 −159 −163 2358 4 −93 −106 1712 0 8 −8 667 −4 106 93 −379 −6 163 159 −1025	−701 8514 −567 7397 −216 4474 216 860 567 −2064 701 −3180

Appendix 3: Choice of truncation level

To determine the number of truncation digits in (35) that preserves shape, we tested a number of challenging CC-nets. Fig. 26 c shows that 3 digits fail: for a simple convex shape of valence 6 shape artifacts appear near the boundary of the bi-4 cap. Compare (c) to (d). Extreme zoom sometimes shows minute 5-digit truncation highlight line jumps near $\mathbf{p}^s_{44} := \hat{\mathbf{c}}$.

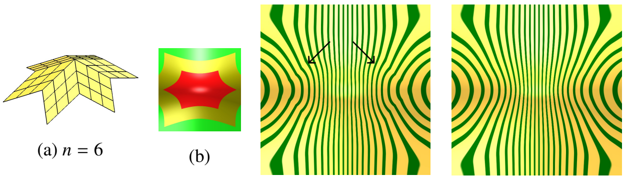

(a) $n = 6$ (b) (c) 3-digit (d) 5-digit

Figure 26: Convex extended CC-net (a) with planar sectors. (b) Layout: bi-4 cap surrounded by a bi-3 ring after one CC-refinement step and the bi-3 patches defined by the planar sectors. (c) 3-digit truncation; ↑ point to artifacts. (d) default 5 digit truncation;

These can be eliminated by overwriting $\mathbf{p}^{s}_{43} = \mathbf{p}^{s+1}_{34}$ with $\tilde{\mathbf{p}}^{s}_{43} := \hat{\mathbf{c}} + \frac{2}{n}\sum_{j=0}^{n-1}\cos(\frac{2\pi}{n}j)\mathbf{p}^{s+j}_{43}$. With subscript 43 replaced by 32 and 34 by 23, the same formulas remove minuscule jumps for a bi-3 cap.